Electronic Supplementary Information (ESI)

High-Purity CH_4 Production from CO_2 via Cascade Electro-Thermocatalysis Using Metal Nanoclusters with High CO_2 Binding Affinity

Sang Myeong Han,[a] Minyoung Park,[a] Seonju Kim,[a] Cheonwoo Jeong,[b] Joonwoo Kim,[b] and Dongil Lee*[a]*

[a] Department of Chemistry, Yonsei University, Seoul 03722, Republic of Korea
[b] Industrial Gas Research Cell, Research Institute of Industrial Science & Technology (RIST), Gwangyang-si 57801, Republic of Korea

.

*Corresponding authors e-mail:

E-mail : realjoon@rist.re.kr (J. K.).

E-mail : dongil@yonsei.ac.kr (D. L.).

Experimental Section

Materials. Silver nitrate ($AgNO_3$, >99.9%), Silver tetrafluoroborate ($AgBF_4$, 99%), 3,3-dimethyl-1-butyne ($HC{\equiv}C^tBu$, 98%), tetrabutylammonium chloride (Bu_4NCl, 95%), tetrabutylammonium fluoride (Bu_4NF, 99%), tetrabutylammonium bromide (Bu_4NBr, >99%), ammonia solution (NH_4OH, 35%), and potassium hydroxide (KOH, >85%) were purchased from Alfa Aesar. Zeolite (chabazite, Si/Al = 16) was purchased from BASF. Hydrogen tetrachloroaurate trihydrate ($HAuCl_4{\cdot}3H_2O$, reagent grade), 1-hexanethiol (HSC_6H_{13}, 98%), n-tetraoctylammonium bromide (TOABr, 98%), sodium borohydride ($NaBH_4$, 99%), Nickel nitrate hexahydrate ($Ni(NO_3)_2{\cdot}6H_2O$, 99.999%), Magnesium nitrate hexahydrate ($Mg(NO_3)_2{\cdot}6H_2O$, 99%), Aluminum nitrate nonahydrate ($Al(NO_3)_3{\cdot}9H_2O$, 99.99%), graphite (powder, 99.99%), and deuterium oxide (D_2O, 99.9 at% D) were purchased from Merck. Extra-pure acetone, dichloromethane (CH_2Cl_2), acetonitrile (CH_3CN), and tetrahydrofuran (THF) were purchased from Merck. High-purity CO_2 and Ar gases were used (>99.999%). Water was purified using a Millipore Milli-Q system (18.2 MΩ·cm). All chemicals were used as received without further purification.

Synthesis of the $Au_{25}(SC_6H_{13})_{18}$ nanoclusters (NCs). The $Au_{25}(SC_6H_{13})_{18}$ NCs (abbreviated as Au_{25}) were synthesized using a previously reported procedure with some modifications.[1] More specifically, $HAuCl_4{\cdot}3H_2O$ (0.196 g, 0.50 mmol) and TOABr (0.317 g, 0.58 mmol) were dissolved in THF (15 mL) in a 100 mL vial. After vigorous stirring for 15 min, the solution color changed from orange to red. Subsequently, 1-hexanethiol (0.320 mL, 2.5 mmol) was slowly added to the above solution over 8 min, and stirring continued for 60 min until the red solution turned colorless. A solution of $NaBH_4$ (0.190 g, 5.0 mmol) dissolved in cold water (5 mL) was then added to the solution, which resulted in bubble evolution and a black solution, indicating the formation of gold clusters. After stirring for an additional 12 h, the aqueous phase was separated using a separating funnel, and the remaining organic phase was washed with fresh water. Compared with the previously reported procedure,[1] the reduction time was increased from 5 to 12 h, significantly increasing the yield of Au_{25} NCs. The resulting oil-like product was washed with methanol and then collected by centrifugation. The washing process was repeated at least 10 times to completely remove any reaction impurities. The purified product was then dissolved in CH_2Cl_2 (10 mL) and transferred to a 250 mL round-bottom flask for rotary evaporation. Au_{25} clusters were repeatedly extracted from the product using a 1:1 (v/v) mixture of acetone/acetonitrile (30 mL). After removing solvent by rotary evaporation, dried Au_{25} clusters were obtained with a typical yield of ~40 mg.

Synthesis of the $ClAg_{14}(C{\equiv}C^tBu)_{12}^+$ NCs. $ClAg_{14}(C{\equiv}C^tBu)_{12}^+$ (abbreviated as Ag_{14}) NCs, where $C{\equiv}C^tBu$ is 3,3-dimethyl-1-butynyl, were synthesized following a previously reported procedure.[2] Briefly, $AgBF_4$ (100 mg, 0.51 mmol) was dissolved in THF (2 mL) containing $HC{\equiv}C^tBu$ (0.054 mL, 0.44 mmol), Bu_4NCl (10 mg, 0.036 mmol), and Et_3N (0.08 mL, 0.52 mmol). Subsequently, the solution was vigorously stirred for 4 h. Following the reaction, the product was washed with copious amounts of water and diethyl ether. Finally, the product was purified via crystallization by layering diethyl ether on the NC solution in CH_2Cl_2. After crystallization, the Ag_{14} NCs were obtained with a typical yield of 80 mg.

Synthesis of thermocatalysts. The catalyst used in this experiment was Ni based Mg/Si/Al zeolite (abbreviated as Ni-zeolite) synthesized by the coprecipitation method according to a previous literature.[3] 9.9 g of nickel nitrate ($Ni(NO_3)_2{\cdot}6H_2O$), 2.6 g of magnesium nitrate ($Mg(NO_3)_2{\cdot}6H_2O$), and 15.0 g of aluminum nitrate ($Al(NO_3)_3{\cdot}9H_2O$) were dissolved in 33.3 mL of water. The solution temperature was raised to 50 °C while stirring the solution using an overhead stirrer. Then, 11.7 mL of aqueous ammonia (NH_4OH solution, 35%) was added dropwise to the solution to precipitate solid particles until pH 7 was reached. After injecting precipitating agent, precipitate

solution was heated to 90 °C. After the reaction was carried out for 3 h, the filtered solid powder was dried at 110 °C overnight. The solid material obtained was calcined at 500 °C for 5 h in a muffle furnace to remove nitrate and ammonium ion. The prepared catalyst was mixed with 0.25 g of binder (graphite, 5 wt%) and 0.5 g of zeolite (chabazite, Si/Al = 16, 10%) and then calcined at 600 °C for 5 h remove graphite. After calcination, 5.0 g of Ni-zeolite catalysts were obtained. Calcined sample was fabricated into pellets with a diameter of 5 mm and a height of 7 mm. These calcined pellets were reduced at 500 °C for 5 h in 5% H_2/N_2 in a reduction furnace and cooled down to ambient temperature. After cooling, reduced sample was passivated in 1% O_2/N_2 to make catalyst surface in oxide state to keep inside particle in reduced one. Passivated sample was pulverized into particles ranging from 200 to 500 µm before being loaded into a fixed-bed reactor.

Characterization of Catalysts. Ultraviolet-visible (UV-Visible) absorption spectra of the NCs were acquired in CH_2Cl_2 using a Shimadzu UV-3600 spectrophotometer. The electrospray ionization (ESI) mass spectra were obtained using an Agilent 6230 TOF LC/MS instrument in the negative- and positive-ion modes for Au_{25} and Ag_{14} NCs, respectively. Au_{25} and Ag_{14} NCs were prepared in CH_2Cl_2 (0.1 mg/mL) and directly injected into the mass spectrometer (Dual AJS ESI system, sample injection rate 0.3 mL/min; gas temperature 250 ℃; nebulizer 1 bar; dry gas 3.0 L/min at 125 ℃; capillary voltage 4000 V; nozzle voltage 500 V; fragmentor voltage 180 V). Transmission electron microscopy (TEM) images were collected on a JEOL electron microscope (JEM-ARM200F NEOARM). TEM samples of Au_{25} and Ag_{14} NCs were prepared by drop-casting the NC solution in CH_2Cl_2 onto a 300-mesh lacey carbon-coated nickel grid without Formvar film (01895N-F, Ted Pella), followed by drying at room temperature for 2 h prior to imaging. TEM samples of the Ni-zeolite catalyst were prepared similarly by drop-casting an ethanol suspension of the pulverized catalyst onto the grid. Powder X-ray diffraction (XRD) data of Ni-zeolite catalyst were collected on a high-resolution X-ray diffractometer (SmartLab, Rigaku).

CO_2 Electrocatalysis. A gas diffusion electrode (GDE, W1S1011, Ce-Tech) was used as a substrate for the NCs. Thus, NC-immobilized GDEs (NC/GDEs) were fabricated using a typical loading of 106 nmol/cm^2, which exhibited the highest catalytic activity. For the fabrication of the NC/GDE, the NCs dissolved in a 1:1 (v/v) mixture of CH_2Cl_2/acetone (1.0 mg/mL) were drop-cast into the microporous layer (MPL) of the GDE. A commercially available cathode, prepared by drop-casting silver nanoparticles onto a GDE (Ag NP/GDE, 4.8 mg/cm^2), was purchased from Dioxide Materials and subsequently used for CO_2 electrocatalysis.

Full-cell measurements for the CO_2-H_2O co-electrolysis were carried out in a zero-gap CO_2 electrolyzer (Figure S2), comprising an NC/GDE cathode (5 cm^2), a Ni foam anode (5 cm^2), and an AEM (Sustainion X37-50, RT grade, Dioxide Materials). CO_2 gas (or Ar gas for hydrogen evolution reaction) was supplied to the cathode via a serpentine flow field, and the fresh 1.0 M KOH electrolyte solution (3 mL/min) was supplied to the anode chamber. Full-cell potentials (E_{cell}) at different current densities were obtained from constant current electrolysis using an MK-W102 programmable DC power supply (MK power, Korea) and ZIVE BP2 electrochemical workstation (WonATech).

A lab-made flow electrolyzer (Figure S4a) consisting of a 2 cm^2 NC/GDE cathode, a 2 cm^2 Ni foam anode (Ni, >99.5%, Goodfellow), and an anion-exchange membrane (AEM, FAAM-40, FuMA-Tech) placed between the two compartments was used for Tafel analysis and kinetic isotope effect study. The constant potential electrolysis (CPE) and electrochemical impedance spectroscopy (EIS) experiments were carried out using a ZIVE BP2 electrochemical workstation (WonATech). The desired potential was applied to the working electrode against a Ag/AgCl reference electrode (1.0 M KCl). Electrode potentials measured on the Ag/AgCl scale ($E_{Ag/AgCl}$) were converted to the standard hydrogen electrode (SHE) scales using the following equations:

$$E_{SHE} = E_{Ag/AgCl} + 0.210$$

Fresh electrolyte was continuously provided at a rate of 1.0 mL/min using a peristaltic pump during the electroreduction of CO_2. CO_2 (or Ar for the hydrogen evolution reaction experiments) was fed at a flow rate of 20 mL/min to the rear side of the GDE cathode.

The amounts of the generated gaseous products, including CO, H_2, CO_2, and CH_4, were quantified using an in-line gas chromatograph (GC 7890B, Agilent) equipped with a thermal conductivity detector and a flame ionization detector. No liquid products were observed in any of the CO_2 electrolysis or thermal methanation reaction experiments in this work.

Electrochemical Syngas Production Using Mixed Catalysts. Co-electrolysis of CO_2 and water into CO and H_2 was evaluated in a zero-gap electrolyzer using a catalyst mixture consisting of CO_2 reduction reaction (CO_2RR)-active and hydrogen evolution reaction (HER)-active catalysts. Au_{25} NCs and a commercially available Pt/C catalyst (20 wt% Pt; 80 wt% Vulcan XC-72 carbon black, Premetek) were used for CO_2RR and HER, respectively.

To achieve specific CO selectivities, different ratios of Pt/C and Au_{25} NC catalysts were immobilized in the MPL of the GDE (W1S1011, Ce-Tech). For 25% CO selectivity, 0.75 mg/cm² of Pt/C and 0.04 mg/cm² of Au_{25} NCs were used. For 50% CO selectivity, the catalyst ratio was adjusted to 0.5 mg/cm² of Pt/C and 0.08 mg/cm² of Au_{25} NCs. For 75% CO selectivity, 0.25 mg/cm² of Pt/C and 0.12 mg/cm² of Au_{25} NCs were employed. A CO selectivity of 90% was achieved using 0.16 mg/cm² of Au_{25} NCs exclusively. CO_2 flow rate was maintained at 30 mL/min throughout these experiments.

Syngas Methanation. Experiments under various operating conditions were conducted in a fixed-bed reactor (inner diameter = 11.2 mm, height = 35 cm). A mesh-type gasket (SS-8-VCR-2-GR-0.5M, 0.5 µm pore, Swagelok) was installed to support the catalyst bed inside the reactor, and 15 g of catalyst was packed in the catalyst bed.

An Ar gas flow of 100 mL/min was maintained until the reactor temperature reached 300 °C, with a temperature ramp rate of 5 °C/min. A K-type thermocouple sensor (SENTECH) was inserted in the middle of the reactor to measure the catalyst bed temperature. The reactor temperature was controlled using a program controller (UP55A, Yokogawa) coupled with an external heating jacket surrounding the reactor.

Calculation of CH_4 Purity in Reported Literature. Purity of CH_4 in the product gas was calculated based on the current density for CH_4 and the product gas selectivity at given CO_2 flow rates. Using the total current and Faradaic efficiency, the molar flow rates of CH_4 and other products were determined. CO_2 losses due to carbonate formation and individual carbon-containing products were subtracted from the initial CO_2 flow rate. Purity of CH_4 was then calculated from the molar flow rates of CH_4, byproducts, and residual gaseous CO_2. Generally, CH_4 purity was primarily influenced by the initial CO_2 flow rate (which is commonly supplied in excess during CO_2 electrolysis) rather than CH_4 selectivity.

Supplementary Notes

Single pass conversion efficiency (SPCE) for syngas production

SPCE of CO_2 was calculated using the following equation:

$$\text{SPCE (\%)} = \frac{i_{CO}/nF}{v/60RT}, \qquad \text{(S1)}$$

where i_{CO} is the CO partial current (mA), n is the number of electrons required for the reaction (2 for CO production), and v is the CO_2 flow rate (mL/min). Other symbols follow their commonly known definitions. Following electrochemical CO_2-to-CO conversion in neutral-alkaline media, the neutralization of CO_2 with OH^- ions occurs as a non-electrochemical reaction:

$$CO_2 + H_2O + 2e^- \rightarrow CO + 2OH^-, \qquad \text{(S2)}$$

$$CO_2 + 2OH^- \rightarrow CO_3^{2-} + H_2O. \qquad \text{(S3)}$$

In other words, when one CO_2 molecule is electrochemically converted to CO, another CO_2 molecule is consumed through a non-electrochemical pathway, producing carbonate ions, thereby limiting the maximum SPCE to 50%. Following Equation S1, the maximum i_{CO} under a CO_2 flow rate of 15 mL/min is calculated to be 1 A for a 5 cm² electrode at a current density of 200 mA/cm². Therefore, decreasing the CO_2 flow rate below 15 mL/min at a current density of 200 mA/cm² for a 5 cm² electrode results in a decreased j_{CO} (and CO selectivity), while j_{H2} increases, maintaining the overall SPCE at 50%. Note that this calculation does not account for carbonate formation associated with the hydrogen evolution reaction (HER), which generates two hydroxide ions for every hydrogen molecule produced from water. If carbonate formation coupled with HER further consumes CO_2, the CO selectivity and corresponding SPCE will decrease below 50% at a given CO_2 flow rate. Theoretically calculated CO_2 flow rates required to achieve target CO selectivity at each current density are listed in Table S1.

Carbon efficiency for cascade electro-thermocatalysis

The carbon efficiency of the cascade system was calculated based on the SPCE of the electrolyzer and the methane fraction in the product stream, as follows:

$$\text{Carbon efficiency (\%)} = \text{SPCE (\%)} \times \frac{[CH_4]}{([CH_4]+[CO_2]+[CO])} \qquad \text{(S4)}$$

Kinetic model for CO_2RR on nanocluster catalysts

Well-defined NCs directly interact with CO_2 in a stoichiometric manner, establishing a quasi-equilibrium with an intermediate. Based on Michaelis-Menten kinetics,[1, 4] the electroreduction of CO_2 to CO ([Eqs. 5–9]) can be simplified into a two-step process as follows:

$$M^* + CO_2 + e^- \underset{k_d}{\overset{k_a}{\rightleftharpoons}} M^*\text{-}CO_2^- \qquad \text{(S5)}$$

$$M^*\text{-}CO_2^- \xrightarrow{k_{cat}} M^* + CO \qquad \text{(S6)}$$

where M* represents the catalytic site, and k_a, k_d, and k_{cat} denote the rate constants for CO_2 adsorption, desorption, and the catalytic reaction, respectively.

The model describes the NC binding to CO_2 to form an intermediate complex, $M^*\text{-}CO_2^-$, which subsequently releases CO as a product, regenerating the catalytic site. Under conditions where the catalyst concentration is significantly lower than that of CO_2, a steady state is rapidly established, ensuring that the concentration of the $M^*\text{-}CO_2^-$ complex remains practically constant on the timescale of product formation. Since Tafel analyses performed on Au_{25} and Ag_{14} NCs revealed that the CO_2RR of these NCs is gated by the second electron transfer step, this model effectively describes the reaction kinetics of the NCs. Consequently, the rate of CO production (v_{CO}) is proportional to the concentration of the $M^*\text{-}CO_2^-$ complex:

$$v_{CO} = k_{cat}\,[M^*\text{-}CO_2^-] \qquad \text{(S7)}$$

The total catalyst concentration ($[M]_0$) is the sum of the free catalyst concentration ([M]) and the concentration of the $[M^*\text{-}CO_2^-]$ complex:

$$[M^*]_0 = [M^*] + [M^*\text{-}CO_2^-] \qquad \text{(S8)}$$

Under the steady-state condition, where $\frac{d[M^*\text{-}CO_2^-]}{dt} = 0$,

$$k_a[CO_2][M^*] = k_a[CO_2]([M^*]_0 - [M^*\text{-}CO_2^-]) = (k_d + k_{cat})[M^*\text{-}CO_2^-] \qquad \text{(S9)}$$

Rearranging Eq. S9 yields

$$[M^*\text{-}CO_2^-] = \frac{K[CO_2][M^*]_0}{1+K[CO_2]} \quad , \qquad \text{(S10)}$$

where $K = \frac{k_a}{k_d+k_{cat}}$ is a measure of the CO_2 binding affinity of a catalyst.

Substituting $[M^*\text{-}CO_2^-]$ in Eq. S7,

$$v_{CO} = \frac{k_{cat}K[CO_2][M^*]_0}{1+K[CO_2]} \qquad \text{(S11)}$$

The rate-determining step involves the second electron transfer step; therefore, j_{CO} is dependent on the applied potential:

$$j_{CO} = \frac{nFk^o_{cat}K[M^*]_0P_{CO_2}}{1+KP_{CO_2}} \exp\left(\frac{\beta\eta F}{RT}\right) \qquad \text{(S12)}$$

where $K = \frac{k_a}{k_d+k_{cat}}$ represents the CO_2 binding affinity constant of the active site, k^o_{cat} is the standard rate constant, β is the symmetry factor, η is the overpotential, and other symbols are as commonly defined.

Supplementary Figures

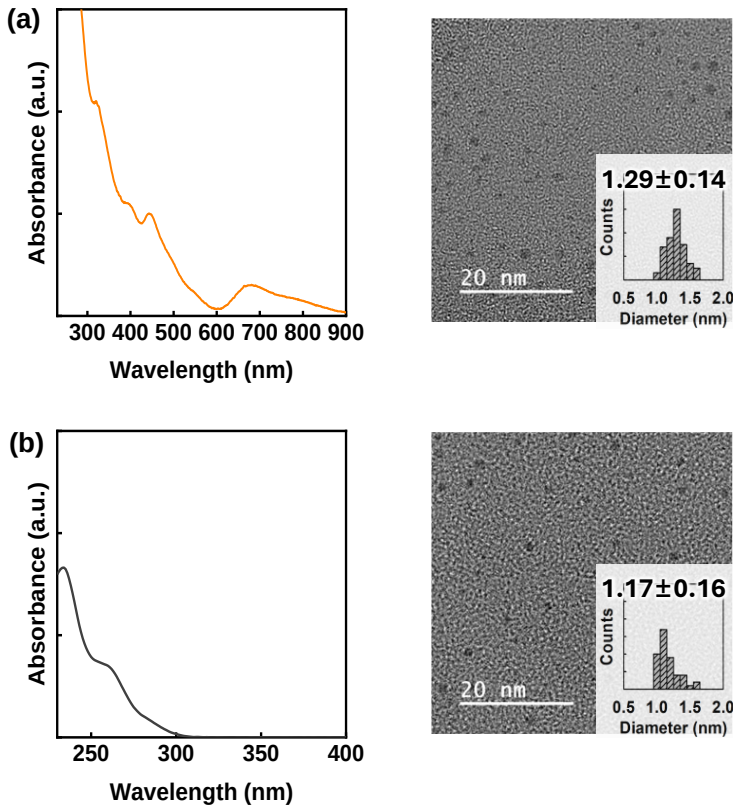

Figure S1. UV-Visible absorption spectra of (a) Au_{25} and (b) Ag_{14} NCs in CH_2Cl_2 (left), along with their corresponding TEM images (right). Insets in the TEM images display histograms of the core diameter distributions.

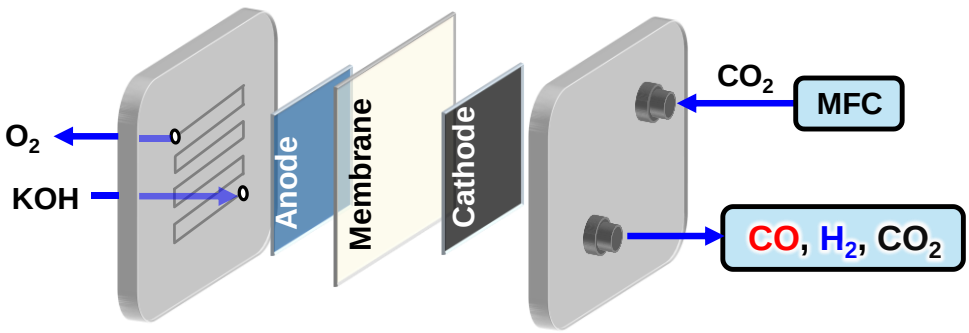

Figure S2. Schematic of a zero-gap electrolyzer. The electrolyzer comprises a GDE-based cathode and an NF anode, with an anion exchange membrane (Sustainion X37-50, RT grade, Dioxide Materials) positioned between the electrodes. During electrolysis, 1.0 M KOH electrolyte was supplied to the anode side. The residual CO_2 and

the product gases (CO and H_2) in the outlet stream were quantified using gas chromatography to monitor the overall carbon conversion efficiency and product gas purity.

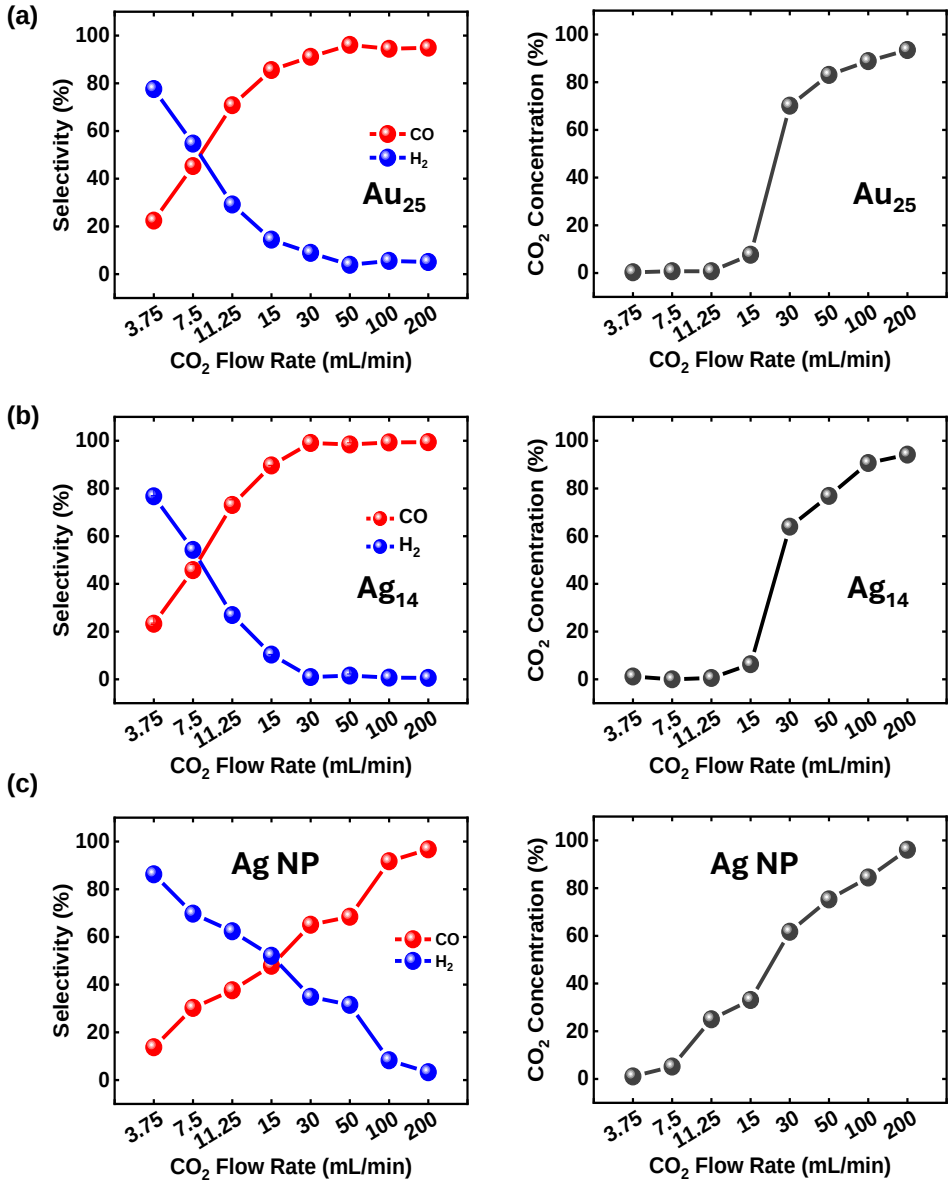

Figure S3. Product gas selectivities (left) and residual CO_2 concentration (right) in the product gas as a function of CO_2 flow rate, obtained from (a) Au_{25} NCs, (b) Ag_{14} NCs, and (c) Ag NPs, recorded during electrolysis at a current density of 200 mA/cm^2.

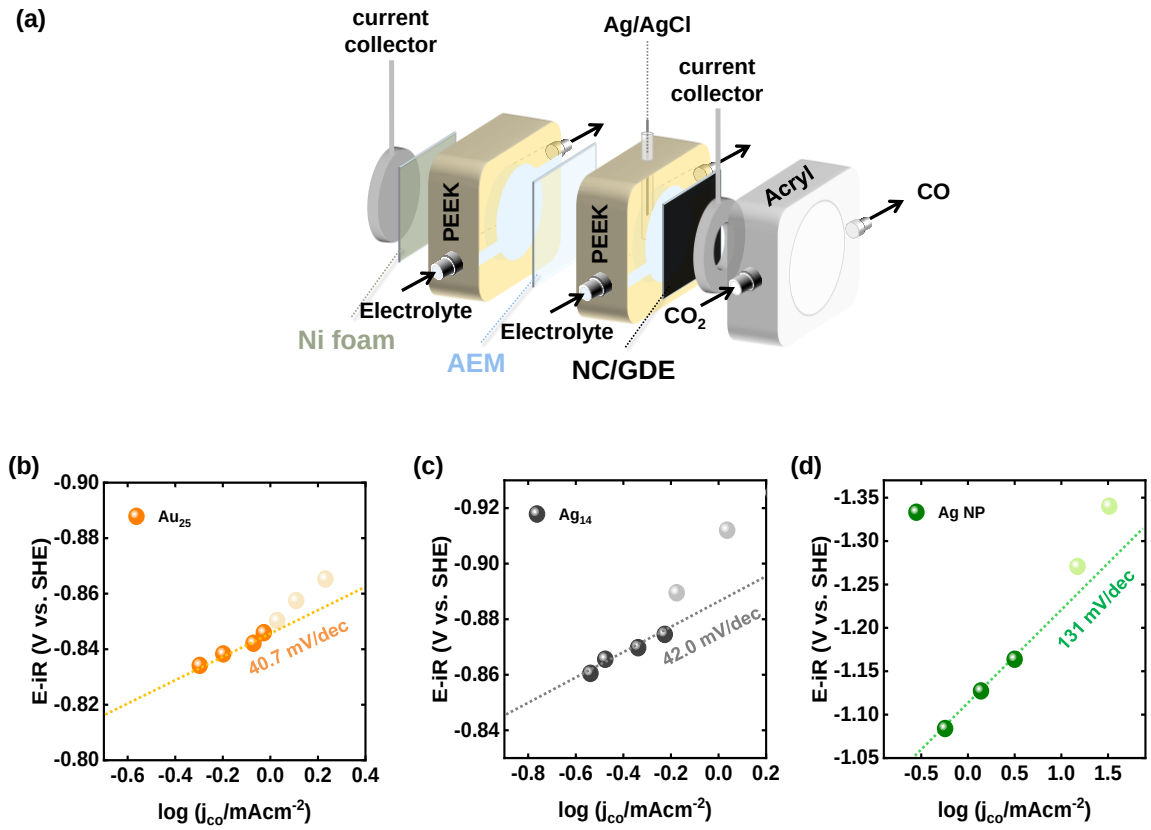

Figure S4. (a) Configuration of the CO_2-fed flow electrolyzer used for the CO_2-to-CO electroreduction process. The flow electrolyzer consists of a 2 cm^2 cathode, a 2 cm^2 anode (Ni foam), and an anion exchange membrane (AEM) placed between the two compartments. CO_2 gas (20 mL/min) was fed to the rear side of the cathode, and fresh electrolyte (1 mL/min) was supplied to the front sides of both electrodes. Potentials applied to the cathode were recorded against the Ag/AgCl (1 M KCl) reference electrode. Tafel plots constructed for the electrochemical CO_2RR on (b) Au_{25} NCs, (c) Ag_{14} NCs, and (d) Ag NPs in a 1.0 M KOH solution. Potentials in panel b-d were iR-corrected.

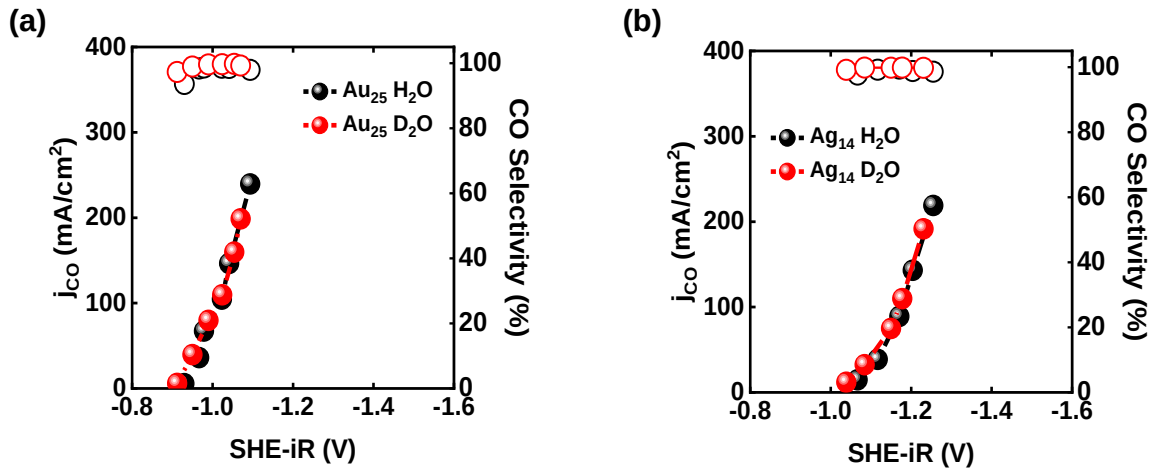

Figure S5. j_{CO} and CO selectivity data obtained in H_2O- and D_2O- based 1.0 M KOH electrolyte solutions on the (a) Au_{25} NCs and (b) Ag_{14} NCs during CO_2RR.

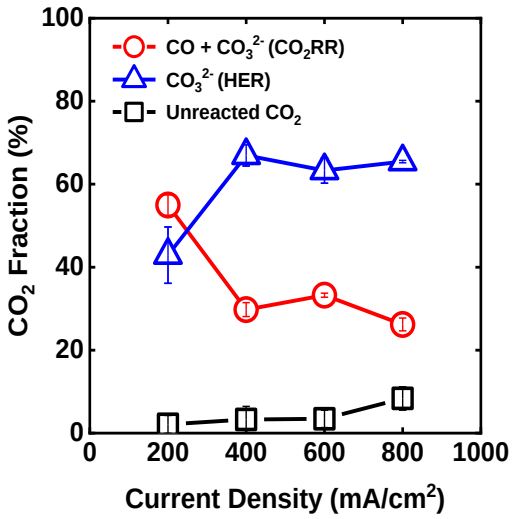

Figure S6. Fractions of CO_2 utilized during syngas production on Ag NPs. $CO+CO_3^{2-}$ (CO_2RR) represents the fraction of CO_2 consumed for CO production and CO_3^{2-} formation, whereas CO_3^{2-} (HER) denotes the CO_2 captured in CO_3^{2-} formation from the HER byproduct. The error bars represent the standard deviation of three separate measurements.

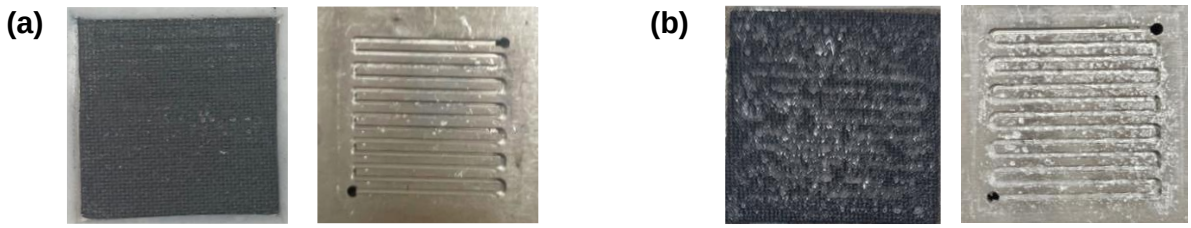

Figure S7. Comparison of digital photographs of the Ag_{14}NCs/GDE backside (left) and the CO_2 flow channel of the zero-gap electrolyzer (right) after electrolysis at 400 mA/cm^2 with a CO_2 flow rate of (a) 8.7 mL/min for 24 h, and (b) 200 mL/min for 1 h.

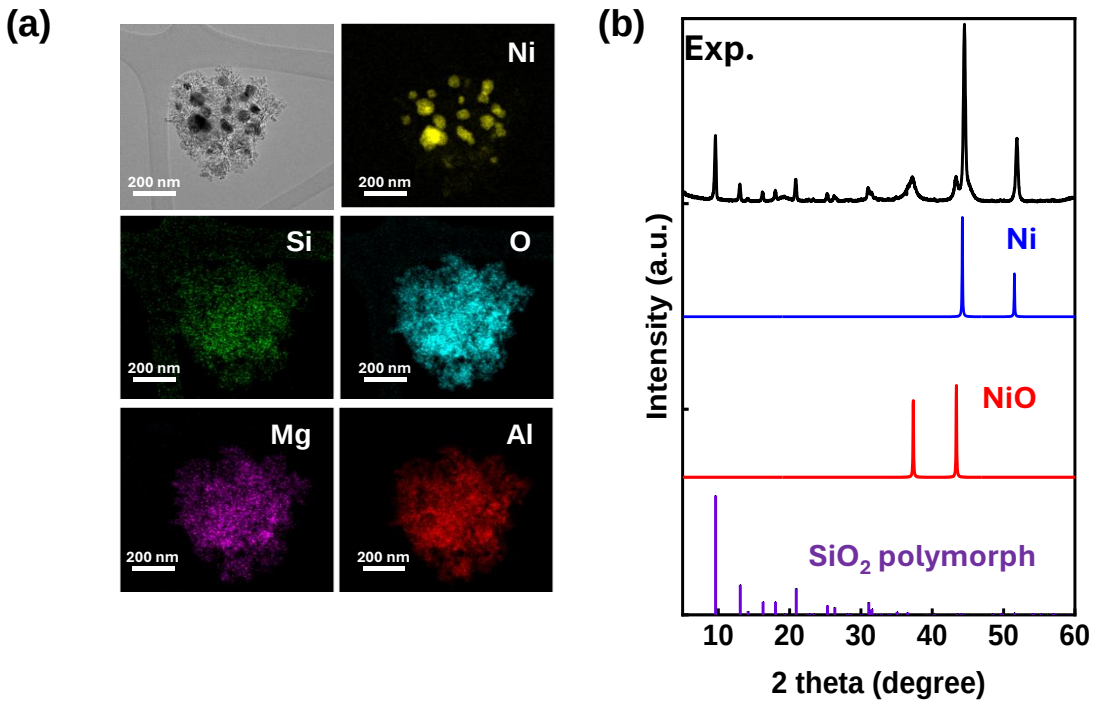

Figure S8. (a) High-resolution TEM and energy dispersive X-ray spectroscopy (EDS) mapping images of the Ni-based Si/Al/Mg zeolite catalyst. (b) XRD patterns of the catalyst (black) and the reference materials: metallic Ni (blue) and NiO (red) and polymorphic SiO_2 (purple).[5]

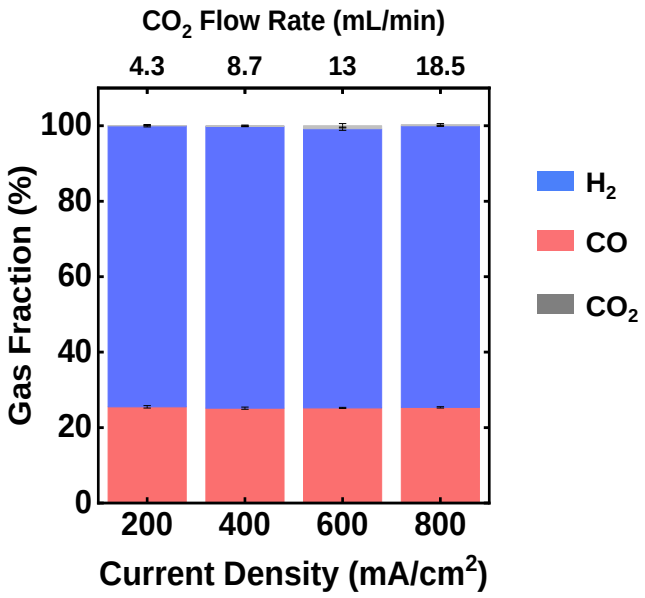

Figure S9. Fractions of the product gas generated from the Ag_{14}-equipped zero-gap electrolyzer. The CO_2 flow rate was adjusted to achieve 25% CO selectivity at each current density.

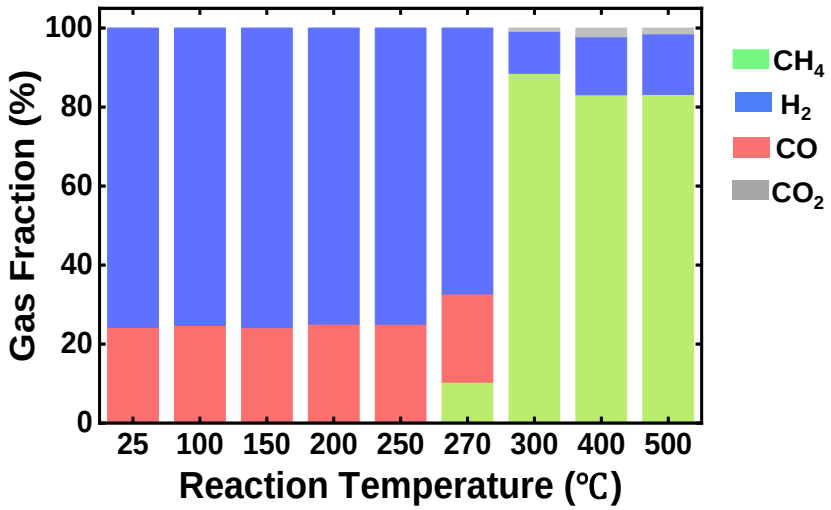

Figure S10. Temperature-dependent syngas-to-CH_4 conversion of the Ni-zeolite catalyst. The fractions of the product gas were recorded after 30 min at each temperature. The syngas flow rate was set to 30 mL/min, with CO and H_2 fractions of 25 and 75%, respectively.

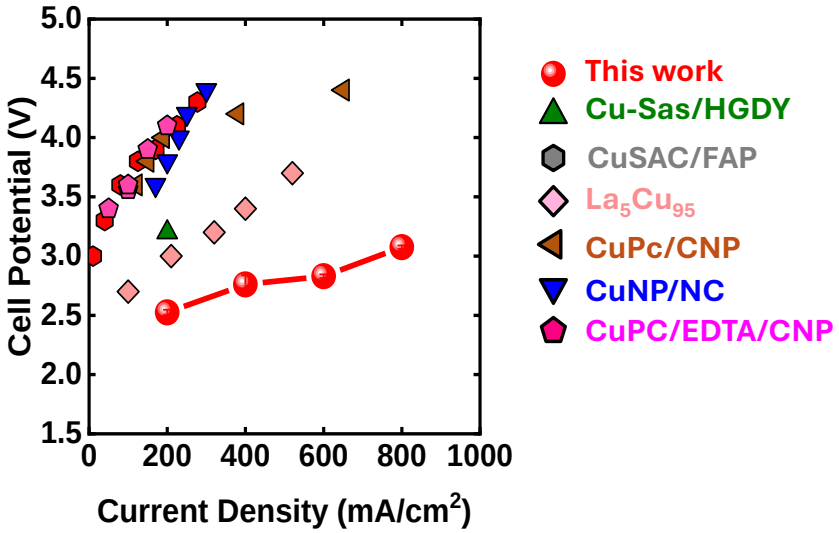

Figure S11. Comparison of cell potentials measured in the Ag_{14}-based cascade electro-thermocatalysis system with those reported in other literature for direct CO_2-to-CH_4 electroreduction.[6-11]

Supplementary Tables

Table S1. Theoretically calculated CO_2 flow rate required to achieve the target CO selectivity at each current density. The SPCE for alkaline CO_2-to-CO electroreduction was assumed to be 50%.

j_{total} (mA/cm^2)	CO_2 flow rate (mL/min)	Converted CO_2 (mL/min, SPCE 50%)	Target selectivity (%)	j_{CO} (mA/cm^2)	j_{H2} (mA/cm^2)	Syngas flow rate (mL/min)
200	3.75	1.875	25	50	150	7.5
400	7.5	3.75	25	100	300	15
600	11.25	5.625	25	150	450	22.5
800	15	7.5	25	200	600	30
200	7.5	3.75	50	100	100	7.5
200	11.25	5.625	75	150	50	7.5
200	15	7.5	100	200	0	7.5

Table S2. Comparison of cell potentials and CH_4 purity in the product gas from the Ag_{14}/GDE-equipped cascade electro-thermocatalysis system with those from direct CO_2-to-CH_4 electrocatalysis system.[6-11]

Catalyst	Ecell (V)	j_{CH4} (mA/cm^2)	FE_{CH4} (%)	*Purity (%)	Electrolyte	Cell type	ref
Ag_{14} Ni-zeolite	3.1	800	-	87	1.0 M KOH	Alkaline MEA	This Work
Cu−SAs/HGDY	3.2	140	70	0.87	1.0 M KOH	Alkaline MEA	*Angew. Chem. Int. Ed.* **2023**, *6 2*, e202314121.
CuSAC/FAP	4.1	166.7	74.1	0.62	0.1 M KOH	Alkaline MEA	Nanoscale **2024**, *16*, 171-179
La_5Cu_{95}	3.4	181.6	45.4	0.82	1 M KOH	Alkaline MEA	*J. Am. Chem. Soc.* **2023**, *145*, 6622
CuPc/CNP	4	117.8	62	0.27	0.05M $KHCO_3$	Neutral MEA	*Nat. Commun.* **2021**, *12*, 2932
Cu-np/NC	4	138	60	0.51	0.1M $KHCO_3$	Neutral MEA	*Chem. Sci.* **2022**, *13*, 8388–8394
CuPc/EDTA/CNP	3.6	71	71	11.12	0.005M H_2SO_4	Acid MEA	*Nat. Commun.* **2023**, *14*, 3314

*The purity of CH_4 was calculated based on the molar CO_2 flow rate, total current density, and product selectivity reported in the literature.

References

1. H. Seong, V. Efremov, G. Park, H. Kim, J. S. Yoo and D. Lee, *Angew. Chem. Int. Ed.*, 2021, **60**, 14563-14570.
2. H. Seong, K. Chang, F. Sun, S. Lee, S. M. Han, Y. Kim, C. H. Choi, Q. Tang and D. Lee, *Adv. Sci.*, 2023, DOI: 10.1002/advs.202306089, 2306089.
3. C. E. Yeo, M. Seo, D. Kim, C. Jeong, H. S. Shin and S. Kim, *Energies*, 2021, **14**, 8414.
4. B. Kim, H. Seong, J. T. Song, K. Kwak, H. Song, Y. C. Tan, G. Park, D. Lee and J. Oh, *ACS Energy Lett.*, 2020, **5**, 749-757.
5. M. J. Díaz-Cabañas, P. A. Barrett and M. A. Camblor, *Chem. Commun.*, 1998, DOI: DOI 10.1039/a804800b, 1881-1882.
6. P. Zhao, H. Jiang, H. Shen, S. Yang, R. Gao, Y. Guo, Q. Zhang and H. Zhang, *Angew. Chem. Int. Ed.*, 2023, **62**, e202314121.
7. Y. Wu, C. Chen, X. Yan, R. Wu, S. Liu, J. Ma, J. Zhang, Z. Liu, X. Xing, Z. Wu and B. Han, *Chem. Sci.*, 2022, **13**, 8388-8394.
8. Y. Xu, F. Li, A. Xu, J. P. Edwards, S. F. Hung, C. M. Gabardo, C. P. O'Brien, S. Liu, X. Wang, Y. Li, J. Wicks, R. K. Miao, Y. Liu, J. Li, J. E. Huang, J. Abed, Y. Wang, E. H. Sargent and D. Sinton, *Nat. Commun.*, 2021, **12**, 2932.
9. J. Li, Y. Jiang, J. Li, X. Wang, H. Liu, N. Zhang, R. Long and Y. Xiong, *Nanoscale*, 2023, **16**, 171-179.
10. M. Fan, R. K. Miao, P. Ou, Y. Xu, Z. Y. Lin, T. J. Lee, S. F. Hung, K. Xie, J. E. Huang, W. Ni, J. Li, Y. Zhao, A. Ozden, C. P. O'Brien, Y. Chen, Y. C. Xiao, S. Liu, J. Wicks, X. Wang, J. Abed, E. Shirzadi, E. H. Sargent and D. Sinton, *Nat. Commun.*, 2023, **14**, 3314.
11. J. Zhao, P. Zhang, T. Yuan, D. Cheng, S. Zhen, H. Gao, T. Wang, Z. J. Zhao and J. Gong, *J. Am. Chem. Soc.*, 2023, **145**, 6622-6627.